# Locating Sources of Oscillations Induced by Control of Voltage Source Converters Based on Energy Structure and Nonlinearity Detection

Zetian Zheng, *Student Member*, *IEEE*, Shaowei Huang, *Member*, *IEEE*, Jun Yan, Qiangsheng Bu, Chen Shen, *Senior Member*, *IEEE*, Mingzhong Zheng, and Ye Liu, *Student Member*, *IEEE*

***Abstract*—The oscillation phenomena associated with the control of voltage source converters (VSCs) are concerning, making it crucial to locate the sources of such oscillations and suppress the oscillations. Therefore, this paper presents a location scheme based on the energy structure and nonlinearity detection. The energy structure, which conforms to the principle of the energy-based method and dissipativity theory, is developed to describe the transient energy flow for VSCs, based on which a defined characteristic quantity is implemented to narrow the scope for locating the sources of oscillations. Moreover, based on the self-sustained oscillation characteristics of VSCs, an index for nonlinearity detection is applied to locate the VSCs that produce the oscillation energy. The combination of the energy structure and nonlinearity detection distinguishes the contributions of different VSCs to the oscillation. The results of a case study implemented by the PSCAD/EMTDC simulation validate the proposed scheme.**

***Index Terms*—Double-loop proportional-integral (PI) control, energy structure, Hamiltonian model, nonlinearity detection, oscillation source location (OSL), voltage source converter (VSC).**

## I. Introduction

In modern power systems, voltage source converters (VSCs) are among the most common power electronic devices. Typical application scenarios of VSCs range from renewable energy generation such as in wind power generation to high-voltage DC and flexible AC transmission systems [1]-[3]. The existing literature [3]-[8] shows that with the high penetration of power converters, dynamic characteristics of power systems have undergone drastic changes, leading to the emergence of oscillatory phenomena, threatening the system stability. Some of these phenomena are associated with the control of VSC.

Across industry and academia, an established consensus is that oscillation source location (OSL) is a crucial measure to suppress oscillation [9], [10]. Correspondingly, in [11], numerous methods for OSL are surveyed and categorized. The most notable is the energy-based method (EBM) [12], which tracks the system-wide energy flow to locate the sources of oscillations. The advantages of the EBM include the following: ① compared with the OSL methods based on damping torque analysis or mode shape estimation, the EBM is adapted to locate forced oscillations and poorly damped oscillations [11]; ② the EBM is convenient for voltage/current measurements in wide-area networks [12], [13]. With the rapid development of phasor measurement units (PMUs), the EBM has been successfully used for oscillation monitoring in actual power systems [14]. Thus, we focus on the EBM, considering its prospects for industrial applications.

In recent years, the EBM has undergone several developments. For example, [13] proposed a distributed cooperative scheme to locate a forced oscillation source by detecting a cut-set energy flow. Moreover, certain studies have focused on the oscillations associated with wind farms. Reference [15] developed an equipment-level location method for low-frequency oscillation sources in power systems with doubly-fed induction generator (DFIG) integration, based on an energy correlation topology network and dynamic energy flow. Reference [16] presented a forced OSL and participation assessment method for DFIGs by analyzing the energy flow, and based on the analysis, the participation factor for oscillations was proposed. In reviewing [13], [15], and [16], the formulas for energy flow, which are suitable for low-frequency OSL, were derived from [12] and proven in [17] and [18] to conform to the dissipativity theory. However, [4] and [6] indicated a risk of sub-synchronous oscillations (SSOs) in multi-VSC systems; therefore, the transient energy flow (TEF) analysis under the SSO condition is crucial for OSL incluced by the control of VSC.

To date, the TEF problem has attracted the interest of several scholars. In [19], a criterion for identifying the source of SSOs was proposed based on TEF, which considered the control interaction between the converter-based wind turbine generators and weak AC grids. Reference [20] presented the

Manuscript received: February 17, 2023; revised: July 15, 2023; accepted: December 17, 2023. Date of CrossCheck: December 17, 2023. Date of online publication: January 2, 2024.

This work was supported by the State Grid Guide Project (No. 5108-202218030A-1-1-ZN).



Z. Zheng, S. Huang, J. Yan, C. Shen (corresponding author), and Y. Liu are with the State Key Laboratory of Power Systems, Department of Electrical Engineering, Tsinghua University, Beijing 100084, China (e-mail: zzt_thu@qq.com; huangsw@tsinghua.edu.cn; 458783027@qq.com; shenchen@mail.tsinghua.edu.cn; liuye18@mails.tsinghua.edu.cn).

Q. Bu and M. Zheng are with State Grid Jiangsu Electric Power Co., Ltd. Research Institute, Nanjing 211103, China (e-mail: tc16002315@163.com; mingzhongz@tju.edu.cn).

DOI: 10.35833/MPCE.2023.000101

formulas for TEF and studied the relationship between the energy flow and damping torque by focusing on the SSO associated with the control of VSC in direct-drive wind farms. However, the formulas for TEF employed in the aforementioned studies are not accompanied by proof of conformance to the dissipativity theory. In other words, the TEF problem has not been fully addressed yet.

In addition, some researchers have examined the nonlinear characteristics of VSC in the SSOs. According to [4] and [21], a VSC-based wind farm may cause a sustained SSO when the control limit is satisfied; evidently, the control limit possesses nonlinear characteristics. In [21], the describing function method was adopted to analyze the nonlinearity of the VSC control limit; however, the relevant nonlinearity detection and OSL were not discussed for the oscillation associated with the limitation of the control of VSC. Additionally, [19] classified the external characteristics of the aforementioned oscillation as an inter-harmonic source and developed a framework for SSO identification considering the harmonic characteristics; however, the result obtained in [19] did not support the distinction of oscillation responsibility among multiple sources. Reference [22] tried to combine OSL and nonlinear detection based on the instantaneous energy supply on port (ESP) and higher order statistics, but failed to explain the applicability of instantaneous values instead of phasors in the energy function.

Therefore, this paper presents a scheme for the OSL induced by the control of VSC based on the energy structure and nonlinearity detection. Accordingly, the energy structure, which is based on the principle of the EBM and conforms to the dissipativity theory, is established to describe the TEF for VSCs. Moreover, the nonlinearity detection method is applied to supplement the identification of oscillation responsibility. The main contributions of this paper are as follows.

1) An equipment-level energy structure is established based on the Hamiltonian model for the VSC, including the main circuit and control loops. Based on the established energy structure, oscillation monitoring can be implemented using a defined characteristic quantity derived from the energy function. Furthermore, this characteristic quantity can be easily obtained using instantaneous voltage/current measurements.

2) Voltage disturbances can induce nonlinear oscillations, considering the limitation characteristic of the control of VSC, an index $\mu$ is introduced for nonlinearity detection to distinguish nonlinear oscillation from the linear one.

3) A novel scheme for OSL is proposed targeting the oscillation caused by the control of VSC. First, the instantaneous voltages and currents are measured to monitor the oscillation. Once the oscillation occurs, oscillation source searching based on the characteristic quantity $\Delta ESP_{\mathrm{ac}}$ is triggered to determine the zones or nodes that produce the oscillating energy to narrow the node scope for the OSL. The Hamiltonian storage functions $H_{VL}$ and $H_{CL}$ for the control of VSC are used to further identify and locate the sources of oscillation. Finally, the nonlinearity detection is applied to determine the oscillation type and identify the oscillation responsibility.

The remainder of this paper is organized as follows. Section II introduces the overall framework of OSL. Section III presents the Hamiltonian model and energy structure for VSC. Section IV discusses the methodology of nonlinearity detection for determining the oscillation type. Section V proposes a scheme for OSL. The feasibility of the proposed scheme, discussed using a case study, is described in Section VI. Finally, conclusions are drawn in Section VII.

## II. Overall Framework of OSL

As shown in Fig. 1, the overall framework of the proposed OSL and analysis method contains the following two steps.

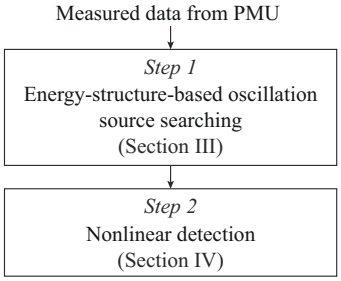


Fig. 1. Flowchart of proposed OSL.

1) Energy-structure-based oscillation source searching: in Section III, the characteristic quantities for oscillation sources are defined by deriving the Hamiltonian model of the main circuit and control loops. Using this method, we can gradually locate the VSCs causing the oscillation.

2) Nonlinear detection: the mechanism and corresponding analysis method of nonlinear oscillations are different from those of linear oscillations [23]. Hence, before choosing the analysis method and adopting the corresponding measures to suppress the oscillation, it is crucial to determine its type (linear or nonlinear) from the waveform records. Section IV analyzes whether the studied oscillation is caused by a nonlinear behavior in the control system by defining a nonlinearity index to examine the flatness of the bicoherence spectrum.

In the following sections, we introduce the two steps in detail.

## III. Hamiltonian Model and Energy Structure for VSC

This section presents the port-controlled Hamiltonian (PCH) model for the VSC and illustrates the corresponding energy structure, which is the basis for monitoring and locating the oscillation sources.

### A. Main Circuit of VSC

Figure 2 illustrates the topology of three-phase VSC, where $v_{\mathrm{a}}$, $v_{\mathrm{b}}$, and $v_{\mathrm{c}}$ are the three-phase voltages at the point of common coupling (PCC); $e_{\mathrm{a}}$, $e_{\mathrm{b}}$, and $e_{\mathrm{c}}$ are the AC-side voltages of the VSC; $v_{\mathrm{dc}}$ is the DC-side voltage of the VSC; $i_{\mathrm{a}}$, $i_{\mathrm{b}}$, and $i_{\mathrm{c}}$ are the three-phase currents of the VSC; $i_{\mathrm{dc}}$ is the DC-side current; $C_{\mathrm{dc}}$ is the DC capacitor; $i_{\mathrm{C}}$ is the current of capacitor; $E_{\infty}$ is the voltage of AC-side infinite bus;

and $R_{ac}$ and $L_{ac}$ are the AC-side equivalent resistance and reactance, respectively.

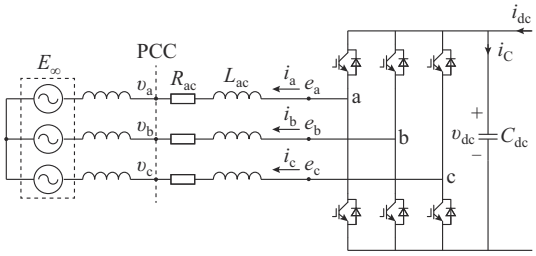


Fig. 2. Topology of three-phase VSC.

The state equations for the main circuit of the VSC can be described as:

$$\begin{cases} L_{ac}\dfrac{\mathrm{d}i_j}{\mathrm{d}t} = e_j - v_j - R_{ac}i_j \quad j=\mathrm{a,b,c} \\ C_{dc}\dfrac{\mathrm{d}v_{dc}}{\mathrm{d}t} = -\left(s_a i_a + s_b i_b + s_c i_c\right) + i_{dc} \end{cases} \tag{1}$$

where $s_a$, $s_b$, and $s_c$ are the switching functions of the VSC. If $s_j=1$, the upper arm of phase $j$ is turned on and the lower arm is turned off; conversely, if $s_j=0$, the situation is reversed.

According to the principle of pulse-width modulation (PWM) and Hamiltonian theory, if we have:

$$e_j = s_j v_{dc} - \frac{\left(s_a+s_b+s_c\right)v_{dc}}{3} = T_j v_{dc} \tag{2}$$

Then, (1) could be turned into:

$$\begin{cases} \dot{\boldsymbol{x}} = (\boldsymbol{J}-\boldsymbol{R})\dfrac{\partial H(\boldsymbol{x})}{\partial \boldsymbol{x}} + \boldsymbol{G}\boldsymbol{u} \\ \boldsymbol{y} = \boldsymbol{G}^{\mathrm{T}}\dfrac{\partial H(\boldsymbol{x})}{\partial \boldsymbol{x}} \end{cases} \tag{3}$$

$$\boldsymbol{x} = \begin{bmatrix} x_1 & x_2 & x_3 & x_4 \end{bmatrix}^{\mathrm{T}} = \begin{bmatrix} L_{ac}i_a & L_{ac}i_b & L_{ac}i_c & C_{dc}v_{dc} \end{bmatrix}^{\mathrm{T}} \tag{4}$$

$$H(\boldsymbol{x}) = \frac{x_1^2}{2L_{ac}} + \frac{x_2^2}{2L_{ac}} + \frac{x_3^2}{2L_{ac}} + \frac{x_4^2}{2C_{dc}} \tag{5}$$

$$\boldsymbol{J} = \begin{bmatrix} 0 & 0 & 0 & T_a \\ 0 & 0 & 0 & T_b \\ 0 & 0 & 0 & T_c \\ -T_a & -T_b & -T_c & 0 \end{bmatrix} \tag{6}$$

$$\boldsymbol{R} = \mathrm{diag}\begin{bmatrix} R_{ac} & R_{ac} & R_{ac} & 0 \end{bmatrix} \tag{7}$$

$$\boldsymbol{G} = \mathrm{diag}\begin{bmatrix} -1 & -1 & -1 & 1 \end{bmatrix} \tag{8}$$

$$\boldsymbol{u} = \begin{bmatrix} v_a & v_b & v_c & i_{dc} \end{bmatrix}^{\mathrm{T}} \tag{9}$$

where $H(\boldsymbol{x})$ is the Hamiltonian energy function.

In (7), the matrix $\boldsymbol{R}$ is positive and semi-definite under normal conditions; therefore, $H(\boldsymbol{x})$, as expressed in (5), satisfies:

$$\frac{\mathrm{d}H(\boldsymbol{x})}{\mathrm{d}t} = \boldsymbol{u}^{\mathrm{T}}\boldsymbol{y} - \frac{\partial H^{\mathrm{T}}(\boldsymbol{x})}{\partial \boldsymbol{x}}\boldsymbol{R}\frac{\partial H(\boldsymbol{x})}{\partial \boldsymbol{x}} \le \boldsymbol{u}^{\mathrm{T}}\boldsymbol{y} \tag{10}$$

Thus, the system described in (3)-(9) is dissipative. Furthermore, according to the law of energy conservation and the dissipativity theory, we can obtain the energy structure of the VSC, which shows the characteristics of the TEF flowing through the main circuit of the VSC. Specifically, the derivation process of the energy structure is as follows.

In reviewing (5), we have the derivative function:

$$\dot{H}(\boldsymbol{x}) = L_{ac}i_a\dot{i}_a + L_{ac}i_b\dot{i}_b + L_{ac}i_c\dot{i}_c + C_{dc}v_{dc}\dot{v}_{dc} \tag{11}$$

Substituting (11) into (3), we can obtain:

$$\begin{cases} T_j i_j v_{dc} - L_{ac}i_j\dot{i}_j - R_{ac}i_j^2 = v_j i_j \quad j=\mathrm{a,b,c} \\ \left(T_a i_a + T_b i_b + T_c i_c\right)v_{dc} = v_{dc}i_{dc} - C_{dc}v_{dc}\dot{v}_{dc} \end{cases} \tag{12}$$

In (12), if we set $i_j$ and $v_{dc}$ as the force variables and set the other terms such as $i_{dc}$, $C_{dc}\dot{v}_{dc}$, $T_j i_j$, $L_{ac}\dot{i}_j$, $R_{ac}i_j$, and $v_j$ as the flow variables, the energy structure for the main circuit of the VSC could be obtained, as shown in Fig. 3.

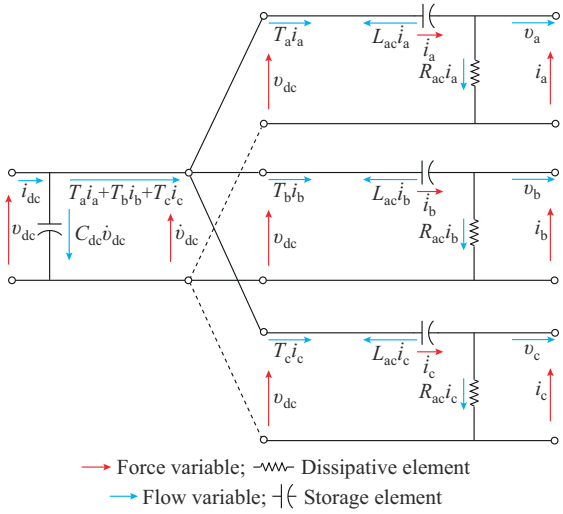


Fig. 3. Energy structure for main circuit of VSC.

From (11), (12), and Fig. 3, the terms $L_{ac}i_j\dot{i}_j$ and $C_{dc}v_{dc}\dot{v}_{dc}$ in the derivative function $\dot{H}(\boldsymbol{x})$ are represented by the storage elements of the energy structure; similarly, in the energy structure, the term $-R_{ac}i_j^2$ in (12) is represented by the dissipative elements. As shown in Fig. 3, the storage energy is equal to the ESP minus the resistive dissipation energy. Therefore, the energy function can be obtained based on the energy-function derivation method presented in [24]:

$$V = \frac{x_1^2}{2L_{ac}} + \frac{x_2^2}{2L_{ac}} + \frac{x_3^2}{2L_{ac}} + \frac{x_4^2}{2C_{dc}} + \int_0^\tau \left(v_a i_a + v_b i_b + v_c i_c - v_{dc}i_{dc}\right)\mathrm{d}t \tag{13}$$

$$\dot{V} = \frac{x_1\dot{x}_1}{L_{ac}} + \frac{x_2\dot{x}_2}{L_{ac}} + \frac{x_3\dot{x}_3}{L_{ac}} + \frac{x_4\dot{x}_4}{C_{dc}} + v_a i_a + v_b i_b + v_c i_c - v_{dc}i_{dc} = -\frac{R_{ac}\left(x_1^2+x_2^2+x_3^2\right)}{L_{ac}^2} \le 0 \tag{14}$$

Evidently, the energy function $V$ can be used to determine the stability of the VSC system; for example, if $R_{ac}$ changes from positive to negative damping under abnormal conditions, then $\dot{V}>0$, and the VSC generates oscillation energy. Therefore, according to (13), the influence of the VSC on AC grids can be investigated by describing the AC-side TEF as:

$$TEF_{\mathrm{ac}}=\int_0^{\tau}\left(v_{\mathrm{a}}i_{\mathrm{a}}+v_{\mathrm{b}}i_{\mathrm{b}}+v_{\mathrm{c}}i_{\mathrm{c}}\right)\mathrm{d}t=\int_0^{\tau}p_{\mathrm{ac}}\mathrm{d}t \tag{15}$$

Equation (15) is equivalent to the ESP at the AC port of the VSC, as shown in Fig. 3. Although the form of (15) is simple, it is derived from the PCH model, which conforms to the dissipativity principle. Furthermore, the characteristic quantity $\Delta ESP_{\mathrm{ac}}$ is defined to monitor the oscillation energy at the AC side of the VSC:

$$\Delta ESP_{\mathrm{ac}}=\int_0^{\tau}\left(p_{\mathrm{ac}}-\bar{p}_{\mathrm{ac}}\right)\mathrm{d}t \tag{16}$$

where $\Delta ESP_{\mathrm{ac}}$ is the accumulation of oscillation energy, and it is suitable for PMU measurement; and $\bar{p}_{\mathrm{ac}}$ is the average value of $p_{\mathrm{ac}}$ during a period.

### *B. Double-loop PI Control of VSC*

In common applications, the VSCs generally adopt the double-loop proportional-integral (PI) control strategy composed of voltage and current control loops, as shown in Fig. 4, where $v_{\mathrm{dcref}}$ and $v_{d\mathrm{ref}}$ are the DC and $d$-axis reference voltages, respectively; $i_{d\mathrm{ref}}$ and $i_{q\mathrm{ref}}$ are the $d$-axis and $q$-axis reference currents, respectively; $K_{\mathrm{P}vd}$, $K_{\mathrm{P}vq}$, and $K_{\mathrm{P}i}$ denote the proportion gains; $e_d$ and $e_q$ are the $d$- and $q$-axis components of the fundamental output voltage of VSC, respectively; and $K_{\mathrm{I}vd}$, $K_{\mathrm{I}vq}$, and $K_{\mathrm{I}i}$ denote the integral gains.

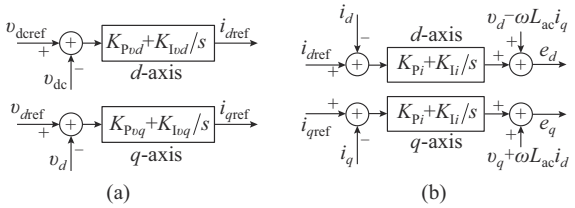


Fig. 4. Block diagrams for voltage and current control loops. (a) Voltage control loop. (b) Current control loop.

Figure 4(a) shows the block diagrams of the voltage control loop, and based on which, we can obtain the corresponding PCH model expressed as:

$$\begin{cases}\dot{\boldsymbol{x}}=\begin{bmatrix}\dot{x}_5\\ \dot{x}_6\end{bmatrix}=\begin{bmatrix}-\dfrac{1}{K_{\mathrm{P}vd}} & 0\\ 0 & -\dfrac{1}{K_{\mathrm{P}vq}}\end{bmatrix}\begin{bmatrix}\dfrac{\partial H_{VL}}{\partial x_5}\\ \dfrac{\partial H_{VL}}{\partial x_6}\end{bmatrix}+\begin{bmatrix}\dfrac{1}{K_{\mathrm{P}vd}} & 0\\ 0 & \dfrac{1}{K_{\mathrm{P}vq}}\end{bmatrix}\boldsymbol{u}\\ \boldsymbol{y}=\begin{bmatrix}\dfrac{1}{K_{\mathrm{P}vd}}\dfrac{\partial H_{VL}}{\partial x_5} & \dfrac{1}{K_{\mathrm{P}vq}}\dfrac{\partial H_{VL}}{\partial x_6}\end{bmatrix}^{\mathrm{T}}\end{cases} \tag{17}$$

$$\begin{cases}x_5=\int\left(v_{\mathrm{dcref}}-v_{\mathrm{dc}}\right)\mathrm{d}t\\ x_6=\int\left(v_{d\mathrm{ref}}-v_d\right)\mathrm{d}t\\ \boldsymbol{u}=\begin{bmatrix}i_{d\mathrm{ref}} & i_{q\mathrm{ref}}\end{bmatrix}^{\mathrm{T}}\end{cases} \tag{18}$$

$$H_{VL}(\boldsymbol{x})=\frac{K_{\mathrm{I}vd}x_5^2}{2}+\frac{K_{\mathrm{I}vq}x_6^2}{2} \tag{19}$$

From (17)-(19), we can obtain:

$$\frac{\mathrm{d}H_{VL}(\boldsymbol{x})}{\mathrm{d}t}=\boldsymbol{u}^{\mathrm{T}}\boldsymbol{y}-\begin{bmatrix}\dfrac{\partial H_{VL}}{\partial x_5}\\ \dfrac{\partial H_{VL}}{\partial x_6}\end{bmatrix}^{\mathrm{T}}\begin{bmatrix}-\dfrac{1}{K_{\mathrm{P}vd}} & 0\\ 0 & -\dfrac{1}{K_{\mathrm{P}vq}}\end{bmatrix}\begin{bmatrix}\dfrac{\partial H_{VL}}{\partial x_5}\\ \dfrac{\partial H_{VL}}{\partial x_6}\end{bmatrix}\le\boldsymbol{u}^{\mathrm{T}}\boldsymbol{y} \tag{20}$$

Hence, the voltage-loop control of the VSC is dissipative. Similar to Section III-A, the corresponding energy structure for the voltage control can be obtained using the PCH model (17), as shown in Fig. 5(a).

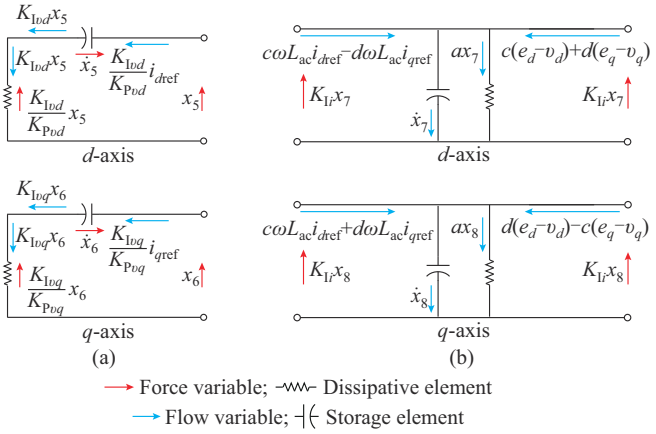


Fig. 5. Energy structure for voltage and current control of VSC. (a) Voltage control. (b) Current control.

The energy structure is consistent with the control strategy, which includes two parts: $d$-axis control and $q$-axis control. Similarly, based on the block diagrams of the current control loop shown in Fig. 4(b), if:

$$\begin{cases}x_7=\int\left(i_{d\mathrm{ref}}-i_d\right)\mathrm{d}t\\ x_8=\int\left(i_{q\mathrm{ref}}-i_q\right)\mathrm{d}t\end{cases} \tag{21}$$

$$H_{CL}(\boldsymbol{x})=\frac{K_{\mathrm{I}i}x_7^2}{2}+\frac{K_{\mathrm{I}i}x_8^2}{2} \tag{22}$$

The corresponding PCH model could be described as:

$$\begin{bmatrix}\dot{x}_7\\ \dot{x}_8\end{bmatrix}=(\boldsymbol{J}-\boldsymbol{R})\begin{bmatrix}\dfrac{\partial H_{CL}}{\partial x_7}\\ \dfrac{\partial H_{CL}}{\partial x_8}\end{bmatrix}+\begin{bmatrix}c & d\\ -d & c\end{bmatrix}\begin{bmatrix}\sigma_d\\ \sigma_q\end{bmatrix} \tag{23}$$

$$\boldsymbol{y}=\begin{bmatrix}c\dfrac{\partial H_{CL}}{\partial x_7}-d\dfrac{\partial H_{CL}}{\partial x_8} & d\dfrac{\partial H_{CL}}{\partial x_7}+c\dfrac{\partial H_{CL}}{\partial x_8}\end{bmatrix}^{\mathrm{T}} \tag{24}$$

$$\begin{cases}\boldsymbol{J}=\begin{bmatrix}0 & \dfrac{-b}{K_{\mathrm{I}i}}\\ \dfrac{b}{K_{\mathrm{I}i}} & 0\end{bmatrix}\\ \boldsymbol{R}=\begin{bmatrix}\dfrac{a}{K_{\mathrm{I}i}} & 0\\ 0 & \dfrac{a}{K_{\mathrm{I}i}}\end{bmatrix}\end{cases} \tag{25}$$

$$\begin{cases}\sigma_d=e_{d\mathrm{ref}}-v_d+\omega L_{\mathrm{ac}}i_{q\mathrm{ref}}\\ \sigma_q=e_{q\mathrm{ref}}-v_q-\omega L_{\mathrm{ac}}i_{d\mathrm{ref}}\end{cases} \tag{26}$$

where $e_{d\text{ref}}$ and $e_{q\text{ref}}$ are the reference voltages of $e_d$ and $e_q$, respectively.

$$\begin{cases} a = \dfrac{K_{\text{I}i}K_{\text{P}i}}{\omega^2 L_{\text{ac}}^2 + K_{\text{P}i}^2} \\ b = \dfrac{\omega L_{\text{ac}}K_{\text{I}i}}{\omega^2 L_{\text{ac}}^2 + K_{\text{P}i}^2} \\ c = \dfrac{a}{K_{\text{I}i}} \\ d = -\dfrac{b}{K_{\text{I}i}} \end{cases} \tag{27}$$

From (23)-(27), we can also obtain the energy structure shown in Fig. 5(b) and verify the dissipativity of the current control loop.

In view of the dissipativity theory, $H_{VL}$ and $H_{CL}$ conform to the essentials of the Lyapunov function [25]. In other words, the continuous increase in $H_{VL}$ and $H_{CL}$ could represent an unstable accumulation of energy accompanied by oscillation. Thus, $H_{VL}$ and $H_{CL}$ can be regarded as characteristic quantities for identifying the oscillation caused by the control of VSC.

## IV. Methodology for Nonlinearity Detection

Section III-A presents the characteristic quantity (16) used to monitor the oscillation energy and locate the sources of oscillation. However, in practice, it is necessary to both locate the sources of oscillations and identify the linear or nonlinear characteristics of oscillations. In this section, we describe the manner in which the nonlinearity is identified and distinguish its intensity.

### *A. Nonlinear Control-loop Performance for VSC*

It was shown in [4] and [21] that the amplitude limit in the control system is related to the oscillation caused by the control of VSC. In this paper, this type of oscillation caused by the control limit is referred to as "control oscillation". Figure 6 illustrates the block diagram of the VSC control system, which conforms to the principle of double-loop PI control described in Section III, where the control limit can be modeled using saturation elements attached to the PI controllers and PWM module. In Fig. 6, $\theta_t$ is the phase angle of the terminal voltage at PCC; and $\theta_p$ is the output of the phase-locked loop (PLL), which traces $\theta_t$ and can be used to specify the angle for the *dq* transformation.

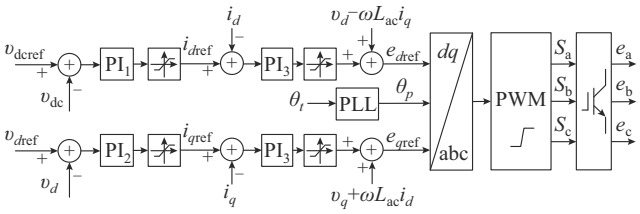


Fig. 6. Block diagram of VSC control system.

Considering that the procedure delay of generating the internal potentials $e_{\text{a}}$, $e_{\text{b}}$, and $e_{\text{c}}$ from the control outputs $e_{d\text{ref}}$ and $e_{q\text{ref}}$ primarily relies on the dynamic of the PLL, the control subsystem composed of the PLL, *dq* transformation, and PWM modules in Fig. 6 could be simplified to a proportion-inertia loop $K_{\text{PWM}}/(\tau_1 s+1)$, where $K_{\text{PWM}}$ is the equivalent gain for the subsystem and $\tau_1$ is the time constant. Additionally, for the control of VSC, the current close-loop tracking between the feedbacks ($i_d$, $i_q$) and references ($i_{d\text{ref}}$, $i_{q\text{ref}}$) can be modeled by the inertia loop with a small time constant $G_{ci}(s) = 1/(\tau_2 s+1)$, because the inner current loop adjusts much faster than the outer voltage loop. Thus, Fig. 7 depicts a simplified closed-loop block diagram for the *d*-axis control of the VSC, where $N_i(A_i)$ $(i=1, 2, 3)$ represent the functions of the saturation elements.

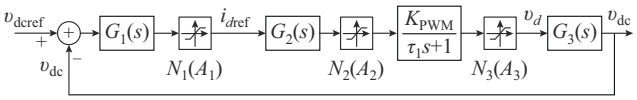


Fig. 7. Simplified closed-loop block diagram for *d*-axis control of VSC.

$$\begin{cases} G_1(s) = K_{\text{P}vd} + K_{\text{I}vd}/s \\ G_2(s) = \left(1 - G_{ci}(s)\right)\left(K_{\text{P}i} + K_{\text{I}i}/s\right) \\ G_3(s) = \dfrac{3v_d/(2v_{\text{dc}})}{3L_{\text{ac}}C_{\text{dc}}s^2/2 + 3R_{\text{ac}}C_{\text{dc}}s/2 + \left[3v_d/(2v_{\text{dc}})\right]^2} \\ N_i(A_i) = 2/\pi\left[\arcsin\left(b_i/A_i\right) + \left(b_i/A_i\right)\sqrt{1-\left(b_i/A_i\right)^2}\right] \end{cases} \tag{28}$$

where $b_i > 0$ is the upper hard limit value; and $A_i$ is the amplitude of sinusoidal input signal of the $i^{\text{th}}$ hard limiter.

In accordance with the principle of harmonic balance for nonlinear oscillation analysis, the system shown in Fig. 7 produces self-sustained oscillations if (29) has a solution.

$$1 + \frac{K_{\text{PWM}}}{\text{j}\tau_1\omega + 1}\prod_{i=1,2,3} G_i(\text{j}\omega)\prod_{i=1,2,3} N_i(A_i) = 0 \tag{29}$$

Further, according to (29), we have:

$$\begin{cases} 20\lg H_l(\omega) = -\sum_{i=1}^{3} 20\lg N_i(A_i) \\ \theta_l(\omega) = -\pi \end{cases} \tag{30}$$

$$\begin{cases} H_l(\omega) = \left|K_{\text{PWM}}/(\text{j}\tau_1\omega+1)\right|\prod_{i=1,2,3}\left|G_i(\text{j}\omega)\right| \\ \theta_l(\omega) = \sum_{i=1}^{3}\arg G_i(\text{j}\omega) + \arg\left(K_{\text{PWM}}/(\text{j}\tau_1\omega+1)\right) \end{cases} \tag{31}$$

If the amplitude- and phase-frequency characteristics of (30) satisfy the inequalities [26], the self-sustained solution $(A_i, \omega_0)$ obtained by (29) is stable.

$$\begin{cases} \dfrac{\text{d}\left(\lg H_l(\omega)\right)}{\text{d}\omega}\Big|_{\omega_0}\sqrt{\dfrac{\text{d}\theta_l(\omega)}{\text{d}\omega}\Big|_{\omega_0}} > 0 \\ \dfrac{\text{d}\left(\lg N_i(a)\right)}{\text{d}a}\Big|_{A_i} < 0 \end{cases} \tag{32}$$

Table I lists the parameters of main circuit and the control of VSC, and Fig. 8 shows the corresponding curves of the amplitude- and phase-frequency characteristics. As shown in

Fig. 8, the linear part of the system exhibits low-pass filtering characteristics, and the frequency of the stable self-sustained solution is 35.7 Hz. Thus, if there is an influence of sustainable voltage disturbance on the control loop shown in Fig. 7, nonlinear oscillations occur because of the control limit.

TABLE I
PARAMETERS OF MAIN CIRCUIT AND CONTROL OF VSC

| Parameter | Value |
|---|---|
| $K_{Pod}$, $K_{Iod}$ | 2.5 p.u., 1000 p.u. |
| $K_{Pi}$, $K_{Ii}$ | 50 p.u., 6250 p.u. |
| $R_{ac}$, $L_{ac}$, $C_{dc}$ | 1.224 Ω, 39.11 mH, 300 μF |
| $K_{PWM}$ | 0.353 p.u. |
| $\tau_1$, $\tau_2$ | 0.00005 p.u., 0.0003 p.u. |

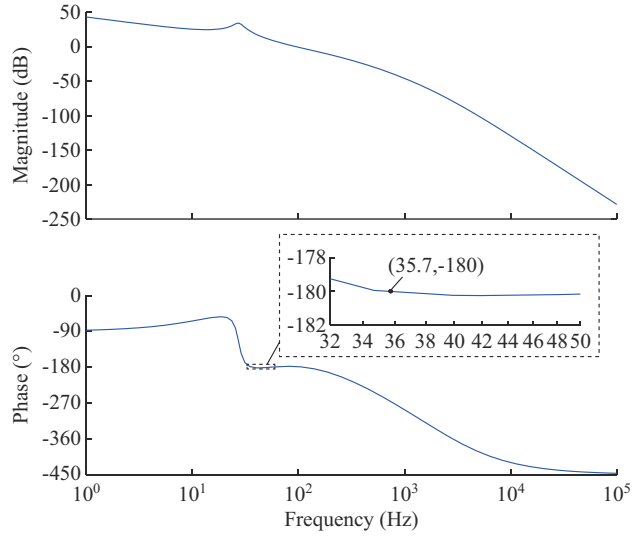


Fig. 8. Corresponding curves of amplitude- and phase-frequency characteristics.

### B. Index μ for Nonlinearity Detection

Figure 7 indicates that the self-sustained oscillation could be observed through the currents of the VSC because the currents are the variables in the forward channel of the control of VSC. As indicated by the timing signal analysis, the oscillatory current of the VSC conforms to the characteristic of a stationary random process $X(n)=A\cos(\Omega n+\Phi)$, where $A$, $\Omega$, and $\Phi$ correspond to independent random variables, and $\Phi$ conforms to the uniform distribution ranging from 0 to $2\pi$. Hence, the mathematical expectation of $X(n)$ is zero [22].

Furthermore, according to the principle of higher-order statistics, the third-order cumulant for the stationary random process $X(n)$, which is understood as the skewness coefficient, can be expressed as:

$$c_{3(X)}(\tau_1,\tau_2)=E\left[X(n),X(n+\tau_1),X(n+\tau_2)\right] \tag{33}$$

If $X(n)$, $X(n+\tau_1)$, and $X(n+\tau_2)$ are independent, we have:

$$c_{3(X)}(\tau_1,\tau_2)=\begin{cases}\gamma_k & \tau_1=\tau_2\\ 0 & \text{otherwise}\end{cases} \tag{34}$$

In (34), it is shown that the cumulant $c_{3(X)}(\tau_1,\tau_2)$ is an impulse function, and because the Fourier transform of the impulse function is a constant, the spectrum of the cumulant $c_3$ is flat. In addition, the cumulant has a linear superposition property, i.e., if the random processes $X(n)$ and $Y(n)$ are independent, the cumulant is expressed as:

$$c_{3(X+Y)}(\tau_1,\tau_2)=c_{3(X)}(\tau_1,\tau_2)+c_{3(Y)}(\tau_1,\tau_2) \tag{35}$$

Thus, if a signal $X(n)$ comprising the sinusoidal fundamental and harmonic components satisfies the linear superposition principle, the cumulant of the signal is equal to the sum of the cumulants for each component, and according to (34), the spectrum of the third-order cumulant for $X(n)$ is flat. However, if a coupling exists between the harmonic components of $X(n)$ such that the signal $X(n)$ is nonlinear (i.e., it does not satisfy the superposition principle), the resulting spectrum of the cumulant $c_{3(X)}$ will not be flat. Hence, the nonlinearity hidden in signal $X(n)$ can be detected using cumulant calculations.

Moreover, in practice, the spectrum of $c_{3(X)}$ is usually defined as a bispectrum $B_X(\omega_1,\omega_2)$ that can be normalized to an absolute scale from 0 to 1, which is called the bicoherence coefficient. The spectra of the bicoherence coefficient and its magnitude are defined as:

$$\begin{cases}K_{2X}(f_1,f_2)=\dfrac{B_X(f_1,f_2)}{\sqrt{P_X(f_1)P_X(f_2)P_X(f_1+f_2)}}\\ bic\triangleq\left|K_{2X}(f_1,f_2)\right|\end{cases} \tag{36}$$

where $f_1$, $f_2$, and $f_1+f_2$ are the frequencies of the Fourier transformation; and $P_X(\cdot)$ is the power spectrum. According to (36), the bicoherence spectrum could reflect a coupling phenomenon between the components at the frequencies $f_1$ and $f_2$. The square of *bic* could be proven to represent the fraction of the power generated by the nonlinear coupling between the components at $f_1$ and $f_2$ to the total power of the component at $f_1+f_2$. Thus, based on the property of cumulant calculation, the criterion of nonlinearity detection for a random process $X(n)$ can be described as follows: if the value of *bic* for $X(n)$ is constant, the process $X(n)$ is linear; otherwise, it is nonlinear. Therefore, a nonlinearity index $\mu$ for verifying the flatness of *bic* could be defined as:

$$\mu\triangleq\left|\hat{K}^2_{2X,\max}-\left(\overline{\hat{K}^2_{2X}}+2\sigma_{\hat{K}^2_{2X}}\right)\right| \tag{37}$$

where $\hat{K}^2_{2X,\max}$ is the estimation of the maximum squared bicoherence; and $\sigma_{\hat{K}^2_{2X}}$ is the variance of $\hat{K}^2_{2X}$. In (37), if $\mu>0$, the signal generating process is nonlinear.

However, the above criterion is theoretically effective, and the actual results obtained by measurements and calculations may violate this criterion. The reasons are as follows. ① The measurement data are a finite-length segment for an actual signal, and the results of *bic* derived from the finite-length data are also affected by the FFT parameter. ② For the power systems, the actual voltages and currents contain background harmonics whose content rates are restricted by the power-quality standards; however, the signals with harmonics would affect the conclusion of the nonlinearity detection. Therefore, a threshold that considers an actual signal

with background harmonics must be discussed.

In this paper, the nonlinearity detection of the control of VSC is based on the measurement of output currents with background harmonics. According to the power-quality standard [27], Table II reports the total harmonic distortion (THD) of load voltage $THD_U$ for 35 kV networks, and the corresponding result of index $\mu$ obtained by simulation is 0.0180. Compared with the result from simulation, the threshold value has a sufficient margin.

TABLE II
THD AND THRESHOLD FOR NONLINEARITY DETECTION

| Harmonic order | $THD_U$ (%) | Result of $\mu$ | Threshold of $\mu$ |
|---|---|---|---|
| 2-25 | 3 | 0.0180 | 0.10 |

## V. PROPOSED SCHEME FOR OSL

To locate the sources of oscillations, the previous sections present the energy structure of the VSC and a nonlinearity index for the control of VSC. Accordingly, this section presents a comprehensive scheme for OSL. Figure 9 illustrates a flowchart of the proposed scheme for OSL.

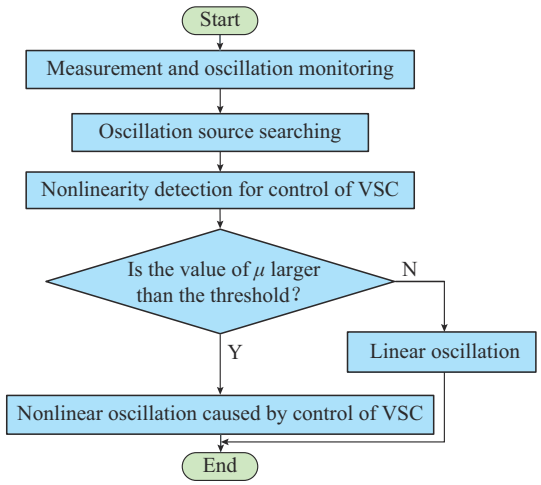


Fig. 9. Flowchart of proposed scheme for OSL.

*Step 1*: measurement and oscillation monitoring. Acquire the sampling sequences of the instantaneous voltages and currents for the VSCs in the system and calculate $\Delta ESP_{ac}$ for each VSC. If $\Delta ESP_{ac,i}$ increases continuously, it is demonstrated that $VSC_i$ injects energy into the AC network and contributes to the increase in energy storage in the power system. Therefore, it can stimulate or maintain the oscillation of the system. Record those nodes of VSCs, and then proceed to *Step 2*.

*Step 2*: oscillation source searching. Analyze the Hamiltonian storage functions $H_{VL}$ and $H_{CL}$ of the VSC nodes selected in *Step 1*. If the values of $H_{VL,j}$ and $H_{CL,j}$ increase continuously, determine $VSC_j$ as a control-induced oscillation source. To further determine the oscillation type (linear or nonlinear), go to *Step 3*.

*Step 3*: nonlinearity detection for the control of VSC. Determine whether the nonlinear oscillation occurs for the VSC. Based on the OSL result obtained in *Step 2*, calculate the value of the nonlinearity index $\mu$ by measuring the output current of the VSC. If the $\mu$ value for the VSC is larger than the threshold, the oscillation associated with the VSC is nonlinear.

## VI. CASE STUDY

Compared with the existing literature, the proposed scheme of OSL for VSC exhibits the following distinguishing features. ① $\Delta ESP_{ac}$ associated with TEF is used to monitor the oscillation and narrow the node scope for the OSL. ② The Hamiltonian energy of the control of VSC is applied to search the VSCs that produce energy in the lower-level networks, cooperating in the method of TEF. ③ Nonlinearity detection is involved in determining the oscillation type, i.e., linear or nonlinear oscillation. The following case study focuses on these aspects.

Figure 10 illustrates the topology of the case study system derived from the IEEE 9-bus system, where the parameters of the network composed of buses 1 to 9 are consistent with the IEEE 9-bus system. In contrast to the IEEE benchmark system, the case study system shown in Fig. 10 locates an static var compensator (SVC) at medium-voltage bus 13 for reactive power adjustment, and grid-connected wind farms and their corresponding static var generators (SVGs) are located at buses 14 and 15. The SVGs adopt double-loop PI control, as described in Section III-B, and the corresponding control parameters are listed in Table III.

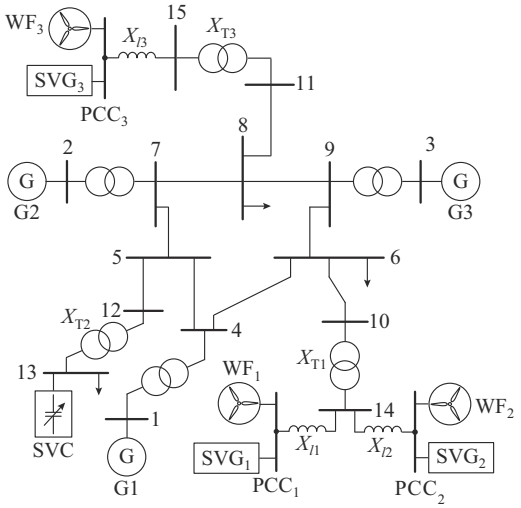


Fig. 10. Topology of case study system.

The case study system is implemented using PSCAD/EMTDC simulation. Figure 11 illustrates the waveforms of the voltages and currents. As shown in Fig. 11(a), when $t<2$ s, the voltage amplitudes $V_{14}$, $E_{SVG1}$, $E_{SVG2}$, and $E_{SVG3}$ are stable; by contrast, when $t\geq 2.45$ s and $V_{ref1}\neq V_{ref2}$, $V_{14}$ deviates from the previous equilibrium point, which fluctuates divergently and finally ranges from 0.97 to 1.04 p.u. owing to the influence of hard limiting. Meanwhile, as indicated in Fig. 11(b), the amplitude of the current $i_{14}$ increases significantly when $t\geq 2.45$ s, and the THD of $i_{14}$ reaches 249.11%.

The major harmonic frequencies of the instantaneous current $i_{14}$ are 17.5 and 82.5 Hz ($50\pm 32.5$ Hz). Thus, it is demonstrated that a sub-synchronous current injection flows from VSCs to networks.

TABLE III
PARAMETERS OF NETWORK AND CONTROL OF VSC FOR CASE STUDY SYSTEM

| Parameter | Value |
|---|---|
| $K_{Pvd}$, $K_{Ivd}$, $K_{Pvq}$, $K_{Ivq}$ (p.u.) | 2.5, 1000, 2, 20 |
| Reference of terminal voltage control $V_{ref1}$, $V_{ref2}$, $V_{ref3}$ (p.u.) | 1.005, 1.005, 1.005 ($t<2$ s)<br>1.005, 1.000, 1.005 ($t\geq 2$ s) |
| $K_{Pi}$, $K_{Ii}$ (p.u.) | 40, 6250 |
| Connection impedances $X_{l1}$, $X_{l2}$, $X_{l3}$ (p.u.) | 0.0051, 0.0038, 0.0256 |
| Line resistances $R_{6\text{-}10}$, $R_{8\text{-}11}$ (p.u.) | 0.0017, 0.0054 |
| Line impedances $X_{6\text{-}10}$, $X_{8\text{-}11}$ (p.u.) | 0.0092, 0.0178 |
| Transformer impedances $X_{T1}$, $X_{T2}$, $X_{T3}$ (p.u.) | 0.0586, 0.0586, 0.0576 |

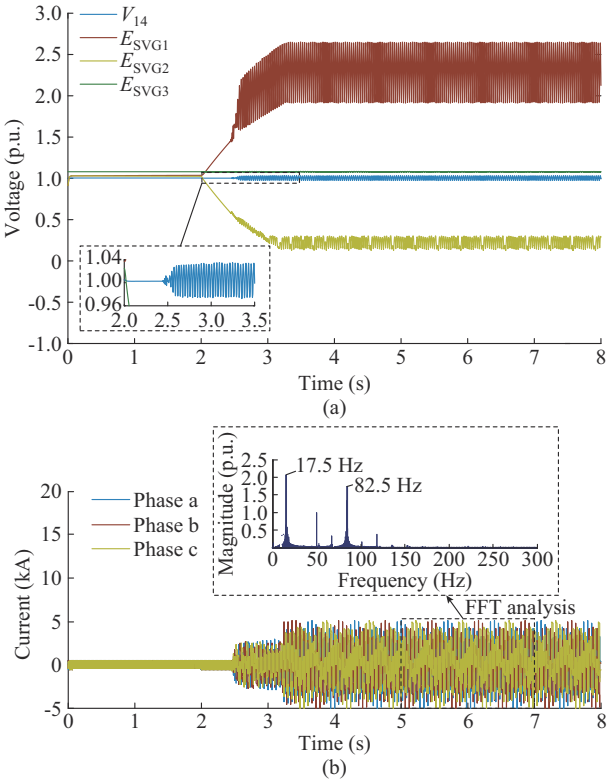


Fig. 11. Waveforms of voltages and currents. (a) Voltage amplitudes. (b) $i_{14}$ and corresponding spectrum with $THD=249.11\%$.

Furthermore, based on (13) and (16), Fig. 12 illustrates the curves of the energy function $V$ for three SVGs and $\Delta ESP_{ac}$ for bus 14. As shown in Fig. 12, when $t\geq 2.45$ s and $V_{ref1}\neq V_{ref2}$, the curves of $V$ for $SVG_1$ and $SVG_2$ both increase and those for $SVG_3$ and WFs remain around zero, which demonstrates that the oscillation energy is produced by $SVG_1$ and $SVG_2$; meanwhile, the curve of $\Delta ESP_{ac}$ also increases when $t\geq 2.45$ s ($\Delta ESP_{ac}>0$), and its growth trend is similar to that of $V$. Thus, $\Delta ESP_{ac}$ can reflect the oscillation properties. Moreover, Fig. 12 shows the curve of another characteristic parameter $W_{TEF}=\int i_x \mathrm{d}v_y - i_y \mathrm{d}v_x$ derived from [20] for each SVG. However, the changing trend of $W_{TEF}$ is not consistent with that of $V$, which fails to describe the oscillation energy flow direction in the system. Hence, the result shown in Fig. 12 verifies the effectiveness of the proposed $\Delta ESP_{ac}$, which can be applied to determine the zone, including the possible SVGs that produce the oscillation energy.

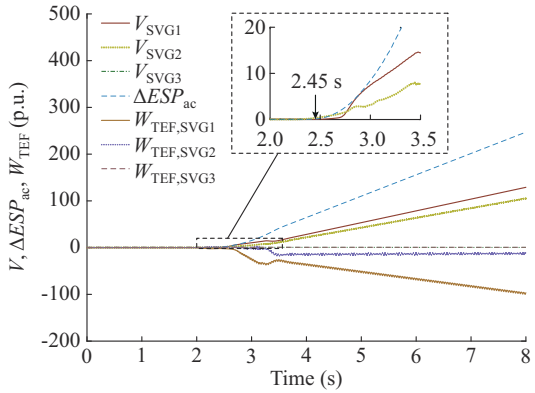


Fig. 12. Curves of energy function $V$ for three SVGs and $\Delta ESP_{ac}$ for bus 14.

Figure 13(a) and (b) shows the waveforms of the Hamiltonian energy and currents. The energy curves indicate that $SVG_1$ and $SVG_2$ produce oscillation energy when $t\geq 2.45$ s because $H_{VL}>0$ and $H_{CL}>0$, and they both show a strong upward trend; by contrast, the Hamiltonian energy of $SVG_3$ is almost equal to zero. $SVG_3$ does not contribute to the oscillation energy, so it is not an oscillation source. It is shown that by cooperating in the identification of $\Delta ESP_{ac}$, the analysis of the Hamiltonian energy could further determine the SVGs where the control oscillation occurs.

Nonlinearity detection is performed using the proposed scheme for OSL, as shown in Fig. 9. As indicated in (5), the Hamiltonian energy of the VSC is related to inductance $L_{ac}$ and capacitance $C_{dc}$. However, the inductance and capacitance elements are extremely common in networks; therefore, it is necessary to distinguish between the LC resonance and VSC control oscillation induced by hard limiting the OSL. Thus, a linear oscillation is triggered to verify the effectiveness of the proposed nonlinearity index. Figure 13(c) shows the current waveform of the SVC at bus 13. The combination of the SVC capacitive reactance and network inductance matches the sub-synchronous frequency of $i_{SVG1}$ and $i_{SVG2}$. Therefore, the SVC stimulates a linear LC resonance. Figure 13(c) shows that the oscillation diverges and the SVC works as a harmonic amplifier.

Table IV presents the comparison of $\mu$ and THD of load current $THD_I$ for harmonic source searching. The values of $\mu$ for $SVG_1$ and $SVG_2$ are significantly higher than that for SVC, implying that both SVGs are the major contributors to the nonlinearity. By contrast, if we locate the nonlinear oscillation sources based on $THD_I$, i. e., the power converter, which produces a self-sustained oscillation, is regarded as a harmonic source, the result will be opposite, because the values of $THD_I$ could not represent the nonlinear characteristic of the oscillation. Thus, the proposed index $\mu$ is beneficial

for filtering the nodes that are definitely linear oscillation sources. To determine which SVG contributes more to the nonlinearity, the result of $\mu$ is compared with the trend of the Hamiltonian energy for $SVG_1$ and $SVG_2$, as shown in Fig. 13(a) and (b), which shows that the converter with a large Hamiltonian energy has a large $\mu$.

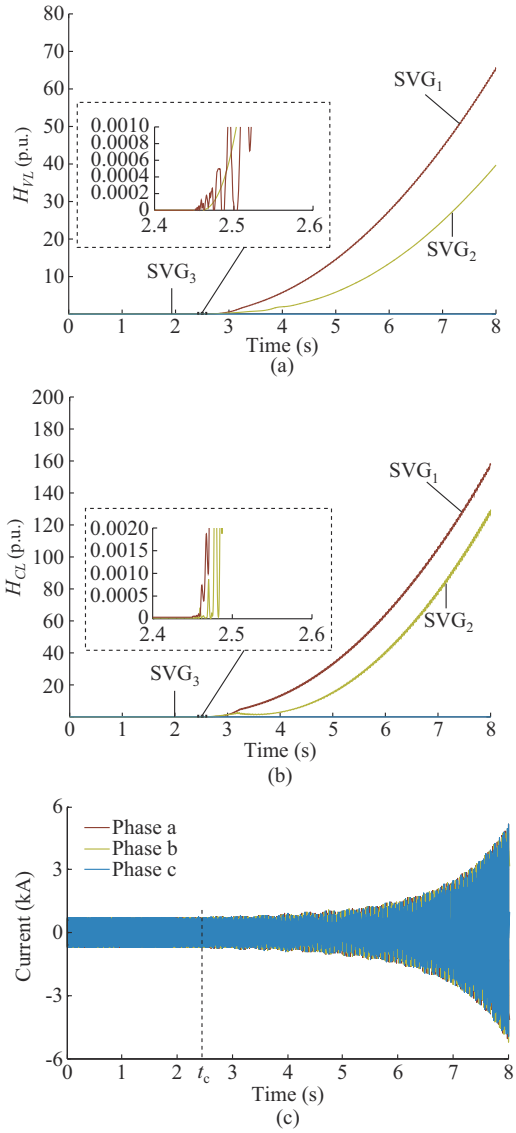


Fig. 13. Waveforms of Hamiltonian energy and currents. (a) $H_{VL}$ for SVG control. (b) $H_{CL}$ for SVG control. (c) Current waveform of SVC.

TABLE IV
COMPARISON OF $\mu$ AND $THD_I$ FOR HARMONIC SOURCE SEARCHING

| Type | $\mu$ (p.u.) | $THD_I$ (%) |
|---|---|---|
| $SVG_1$ | 0.3727 | 77.2610 |
| $SVG_2$ | 0.1598 | 59.5503 |
| SVC | 0.0079 | 385.3142 |

Therefore, the results of the case study confirm that the proposed scheme for OSL can locate the VSCs that cause control oscillations and distinguish the contributions of different converters to the oscillation energy.

## VII. CONCLUSION

We propose a scheme for locating the source of the oscillation caused by the control of the VSC based on the energy structure and nonlinearity detection. First, the energy structure of the VSC is proposed via PCH modeling. Based on the energy structure, $\Delta ESP_{ac}$ is defined to implement the oscillation monitoring and narrow down the node scope for OSL. Moreover, $H_{VL}$ and $H_{CL}$ are applied to determine the converter where the control oscillation occurs. To further determine the type of oscillation and identify the oscillation responsibility, a nonlinearity index and its threshold are discussed. The oscillatory power converter is located based on the proposed scheme for OSL. Finally, the results of a case study implemented using the PSCAD/EMTDC simulation validate the proposed scheme.

## REFERENCES

[1] M. Zou, Y. Wang, C. Zhao *et al.*, "Integrated equivalent model of permanent magnet synchronous generator based wind turbine for large-scale offshore wind farm simulation," *Journal of Modern Power Systems and Clean Energy*, vol. 11, no. 5, pp. 1415-1426, Mar. 2023.

[2] M. Amin and M. Molinas, "Small-signal stability assessment of power electronics based power systems: a discussion of impedance- and eigenvalue-based methods," *IEEE Transactions on Industrial Applications*, vol. 53, no. 5, pp. 5014-5030, Sept. 2017.

[3] Y. Pipelzadeh, N. R. Chaudhuri, B. Chaudhuri *et al.*, "Coordinated control of offshore wind farm and onshore HVDC converter for effective power oscillation damping," *IEEE Transactions on Power Systems*, vol. 32, no. 3, pp. 1860-1872, May 2017.

[4] H. Liu, X. Xie, J. He *et al.*, "Subsynchronous interaction between direct-drive PMSG based wind farms and weak AC networks," *IEEE Transactions on Power Systems*, vol. 32, no. 6, pp. 4708-4720, Nov. 2017.

[5] W. Du, Q. Fu, and H. Wang, "Subsynchronous oscillations caused by open-loop modal coupling between VSC-based HVDC line and power system," *IEEE Transactions on Power Systems*, vol. 33, no. 4, pp. 3664-3677, Jul. 2018.

[6] M. Beza and M. Bongiorno, "On the risk for subsynchronous control interaction in type 4 based wind farms," *IEEE Transactions on Sustainable Energy*, vol. 10, no. 3, pp. 1410-1418, Jul. 2019.

[7] Y. Li, L. Fan, and Z. Miao, "Wind in weak grids: Low-frequency oscillations, subsynchronous oscillations, and torsional interactions," *IEEE Transactions on Power Systems*, vol. 35, no. 1, pp. 109-118, Jan. 2020.

[8] K. Sun, W. Yao, J. Fang *et al.*, "Impedance modeling and stability analysis of grid-connected DFIG-based wind farm with a VSC-HVDC," *IEEE Journal of Emerging and Selected Topics in Power Electronics*, vol. 8, no. 2, pp. 1375-1390, Jun. 2020.

[9] S. C. Chevalier, P. Vorobev, and K. Turitsyn, "Using effective generator impedance for forced oscillation source location," *IEEE Transactions on Power Systems*, vol. 33, no. 6, pp. 6264-6277, Nov. 2018.

[10] S. Chevalier, P. Vorobev, and K. Turitsyn, "A Bayesian approach to forced oscillation source location given uncertain generator parameters," *IEEE Transactions on Power Systems*, vol. 34, no. 2, pp. 1641-1649, Mar. 2019.

[11] B. Wang and K. Sun, "Location methods of oscillation sources in power systems: a survey," *Journal of Modern Power Systems and Clean Energy*, vol. 5, no. 2, pp. 151-159, Mar. 2017.

[12] L. Chen, Y. Min, and W. Hu, "An energy-based method for location of power system oscillation source," *IEEE Transactions on Power Systems*, vol. 28, no. 2, pp. 828-836, Apr. 2013.

[13] X. Wu, X. Chen, M. Shahidehpour *et al.*, "Distributed cooperative scheme for forced oscillation location identification in power systems," *IEEE Transactions on Power Systems*, vol. 35, no. 1, pp. 374-384, Jan. 2020.

[14] S. Maslennikov and E. Litvinov, "ISO New England experience in locating the source of oscillations online," *IEEE Transactions on Power Systems*, vol. 36, no. 1, pp. 495-503, Jan. 2021.

[15] J. Ma, Y. Zhang, Y. Shen *et al.*, "Equipment-level locating of low frequency oscillating source in power system with DFIG integration

based on dynamic energy flow," *IEEE Transactions on Power Systems*, vol. 35, no. 5, pp. 3433-3447, Sept. 2020.
[16] J. Lei, H. Shi, P. Jiang *et al*., "An accurate forced oscillation location and participation assessment method for DFIG wind turbine," *IEEE Access,* vol. 7, pp. 130505-130514, Sept. 2019.
[17] Y. Li, C. Shen, and F. Liu, "An energy-based methodology for locating the source of forced oscillations in power systems," in *Proceedings of IEEE International Conference on Power System Technology*, Auckland, New Zealand, Sept. 2012, pp. 1-6.
[18] S. Chevalier, P. Vorobev, and K. Turitsyn, "A passivity interpretation of energy-based forced oscillation source location methods," *IEEE Transactions on Power Systems*, vol. 35, no. 5, pp. 3588-3602, Sept. 2020.
[19] X. Xie, Y. Zhan, J. Shair *et al*., "Identifying the source of subsynchronous control interaction via wide-area monitoring of sub/super-synchronous power flows," *IEEE Transactions on Power Delivery*, vol. 35, no. 5, pp. 2177-2185, Oct. 2020.
[20] Y. Ren, X. Wang, L. Chen *et al.*, "Component damping evaluation in sub-synchronous oscillation based on transient energy flow method," *IET Generation, Transmission & Distribution*, vol. 14, no. 3, pp. 460-469, Mar. 2020.
[21] Y. Xu, Z. Gu, and K. Sun, "Characterization of subsynchronous oscillation with wind farms using describing function and generalized Nyquist criterion," *IEEE Transactions on Power Systems*, vol. 35, no. 4, pp. 2783-2793, Jul. 2020.
[22] Q. Lu, Z. Zheng, Y. Liu *et al.* (2023, Jan.). Locating sources of subsynchronous oscillations in wind farms based on instantaneous energy supply on port and bicoherence. [Online]. Available: https://iopscience.iop.org/article/10.1088/1742-6596/2625/1/012027.
[23] T. Wu, Q. Jiang, J. Shair *et al.*, "Inclusion of current limiter nonlinearity in the characteristic analysis of sustained subsynchronous oscillations in grid-connected PMSGs," *IEEE Transactions on Energy Conversion*, vol. 36, no. 3, pp. 2416-2426, Sept. 2021.
[24] Y. Li, "Methodology for locating the oscillation sources in power systems based on energy structure," Ph. D. dissertation, Department of Electrical Engineering, Tsinghua University, Beijing, China, 2013.
[25] V. D. Schaft and Arjan, *$L_2$-gain and Passivity Techniques in Nonlinear Control*. London: Springer, 2000, pp. 31-61.
[26] G. Xiang, *Nonlinear Control System*. Beijing: China Electric Power Press, 2014, pp. 56-64.
[27] *Quality of Electric Energy Supply – Harmonics in Public Supply Network*, China National Standard 14549-1993.

**Zetian Zheng** received the B.E. and Ph.D. degrees from the Department of Electrical Engineering, Tsinghua University, Beijing, China, in 2017 and 2023, respectively. He is currently an Engineer with Beijing Institute of Astronautical Systems Engineering, Beijing, China. His research interests include stability analysis and control of power systems containing new energy sources.

**Shaowei Huang** received the B.E. and Ph.D. degrees from the Department of Electrical Engineering, Tsinghua University, Beijing, China, in 2006 and 2011, respectively. From 2011 to 2013, he held a postdoctoral position at the Department of Electrical Engineering, Tsinghua University, where he is currently an Associate Professor. His research interests include power system modeling and simulation, power system parallel and distributed computing, complex systems and its application in power systems, and artificial intelligence.

**Jun Yan** received the B.E. degree in automation engineering and the M.E. degree in electrical engineering from Lanzhou University of Technology, Lanzhou, China, in 2007 and 2011, respectively, and the Ph.D. degree in electrical engineering from the Army Engineering University of PLA, Nanjing, China, in 2018. He worked as a Postdoctor in the Department of Electrical Engineering, Tsinghua University, Beijing, China, from 2019 to 2021. He is currently working as a Lecturer in Army Engineering University of PLA. His research interests include power system dynamics, input-state stability, the energy-structure theory and its application to the oscillation locating.

**Qiangsheng Bu** received the B.E. and M. S. degrees in electrical engineering from Southeast University, Nanjing, China, in 2006 and in 2009, respectively. He is currently working as a Senior Engineer in State Grid Jiangsu Electric Power Co., Ltd. Research Institute, Nanjing, China. His research interests include power system automation, relay protection, and control and protection of distributed new energy.

**Chen Shen** received the B.E. and Ph.D. degrees in electrical engineering from Tsinghua University, Beijing, China, in 1993 and 1998, respectively. From 1998 to 2001, he was a Postdoc Research Fellow with the Department of Electrical Engineering and Computer Science, University of Missouri Rolla, Rolla, USA. From 2001 to 2002, he was a Senior Application Developer with ISO New England, Inc.. Since 2009, he has been a Professor with the Department of Electrical Engineering, Tsinghua University. He is currently the Director of the Energy Digitization Research Center, Sichuan Energy Internet Research Institute, Tsinghua University. His research interests include power system analysis and control, renewable energy generation, and smart grids.

**Mingzhong Zheng** received the Bachelor's degree in electrical engineering and automation from Fuzhou University, Fuzhou, China, in 2011, and the Master's degree in electrical engineering from Tianjin University, Tianjin, China, in 2015. He is currently a Senior Engineer at the State Grid Jiangsu Electric Power Co., Ltd. Research Institute, Nanjing, China. His research interests include integrated energy, microgrids, flexible interconnection, and substation automation.

**Ye Liu** received the B.E. degree in electrical engineering from Wuhan University, Wuhan, China, in 2018, and the Ph.D. degree in electrical engineering from Tsinghua University, Beijing, China, in 2023. He is currently an Engineer with China Huadian Corporation Ltd., Beijing, China. His research interests include stability analysis, optimal control and game theory based decision-making in power systems.